Characteristics of Deep Cloud Systems under Weak and Strong Synoptic Forcing during the Indian Summer Monsoon Season

JAYESH PHADTARE AND G. S. BHAT

Centre for Atmospheric and Oceanic Sciences, and Divecha Centre for Climate Change, Indian Institute of Science, Bengaluru, India

(Manuscript received 9 October 2018, in final form 11 June 2019)

ABSTRACT

Synoptic-scale weather systems are often responsible for initiating mesoscale convective systems (MCSs). Here, we explore how synoptic forcing influences MCS characteristics, such as the maximum size, lifespan, cloud-top height, propagation speed, and triggering over the Indian region. We used 30-min interval infrared (IR) data of the Indian *Kalpana-1* geostationary satellite. Cloud systems (CSs) in this data are identified and tracked using an object tracking algorithm. ERA-Interim 850-hPa vorticity is taken as a proxy for the synoptic forcing. The probability of CSs being larger, longer lived, and deeper is more in the presence of a synoptic-scale vorticity field; however, the influence of synoptic forcing is not evident on the westward propagation of CSs over land. There exists a linear relationship between maximum size, lifespan, and average cloud-top height of CSs regardless of the nature of synoptic forcing. Formation of CSs peaks around 1500 LST over land, which is independent of synoptic forcing. Over the north Bay of Bengal, CSs formation is predominantly nocturnal when synoptic forcing is strong, whereas, 0300 and 1200 LST are the preferred times when synoptic forcing is weak. Long-lived CSs are preferentially triggered in the western flank of the 850-hPa vorticity gradient field of a monsoon low pressure system. Once triggered, CSs propagate westward and ahead of the synoptic system and dissipate around midnight. Formation of new CSs on the next day occurs in the afternoon hours in the wake of previous day's CSs and where vorticity gradient is also present. Formation and westward propagations of CSs on successive days move the synoptic envelope westward.

1. Introduction

Tropical convection (henceforth, convection) exhibits a hierarchy of scales, both spatial (ranging from cumulus to planetary) and temporal (from less than an hour to several days) (Nakazawa 1988). Two important scales in this hierarchy are meso [linear dimension of precipitating area in one dimension is at least 100 km and time scale of a few hours to ~24 h (Houze 1989, 2004)] and synoptic (length scale ~1000 km and time scale a few to ~10 days). Space–time spectra of satellite-derived tropical cloudiness show significant variance at the synoptic scales [e.g., Figs. 6 and 7 in Takayabu (1994)]. Major fraction of total precipitation is produced at the mesoscale and the latent heat released in mesoscale convective systems (MCSs) drives the large-scale tropical atmospheric circulation (Houze 1989). These, along with the other underlying rich physical processes involved motivated a large number of studies on MCSs [Houze (2004) and references therein].

In a slowly evolving synoptic field that facilitates low-level convergence, several MCSs with a lifespan of a few hours to ~24 h form and dissipate. MCS formation is also influenced by the diurnal cycle, over both land and ocean [Johnson (2011) and references therein]. It is known that MJO influences the phase and amplitude of the diurnal cycle of convection over the tropics [Sakaeda et al. (2017) and references therein]. MCSs get triggered over land owing to a combination of strong diurnal heating and local (topographic) features even when synoptic forcing is absent or weak. Their number may be relatively a few but they can cause severe weather over a limited area. Does a strong synoptic forcing produce anomalously large/long-lived MCSs (Machado et al. 1992; Nguyen and Duvel 2008; Berthet et al. 2017) or more number of MCSs without affecting the size/lifespan distribution (Dias et al. 2017)? Basically, how do the characteristics of MCSs (e.g., size, lifespan, and height)

Supplemental information related to this paper is available at the Journals Online website: https://doi.org/10.1175/MWR-D-18-0346.s1.

Corresponding author: Jayesh Phadtare, phadtare@iisc.ac.in

DOI: 10.1175/MWR-D-18-0346.1

that form during the periods of strong and weak synoptic forcing compare? Addressing this question is the main objective of the paper. We also examine the dependence of preferred locations and timings of MCS triggering in relation to the synoptic forcing field.

The paper is organized as follows. Study area, data, and method are described in section 2. Section 3 presents some case studies of evolution of deep convective clouds in the presence of synoptic forcing. Section 4 presents characteristics of deep clouds with strong and weak synoptic forcing. Section 5 contains a discussion on our findings and section 6 concludes the paper.

2. Study area, data, and method

a. Study area

The Indian subcontinent receives about 76% of its annual rainfall during the Indian summer monsoon season (June–September), mainly owing to the frequent formation of synoptic low pressure systems (Sikka 1978; Krishnamurthy and Ajayamohan 2010; Hunt et al. 2016a). Indian summer monsoon is in the transient phase in the months of June and September. July and August are the peak monsoon months (Fig. 1a) and the results here are mainly based on the data of these 2 months. A region of low sea level pressure, called monsoon trough (Rao 1976), lies between 20° and 25°N over the Indian subcontinent during the summer monsoon season. A large number of synoptic-scale systems [viz., monsoon depressions and monsoon lows (e.g., Sikka 1978)] either form or propagate over the monsoon trough. Henceforth, monsoon lows and depressions are referred to as low pressure systems (LPSs). They predominantly form over the northern Bay of Bengal (henceforth, ''Bay'') and then move onto the Indian subcontinent (Sikka 1980; Krishnamurthy and Ajayamohan 2010; Hurley and Boos 2015; Hunt et al. 2016b). As a result, deep convection is frequent over this region (Fig. 1b). Within a summer monsoon season, large-scale conditions fluctuate between active and break periods [Gadgil (2003) and references therein] with the active period characterized by large-scale low-level convergence and enhanced 850-hPa cyclonic vorticity (Sikka and Gadgil 1978). Opposite conditions prevail during the break period. Several active and break periods occur during the season.

Above facts and the availability of high temporal resolution geostationary satellite data for the region provide an ideal opportunity to address our objectives. We have selected the area 15°–25°N, 75°–91°E, henceforth referred to as ''monsoon zone,'' which encompasses monsoon trough and part of northern Bay (Fig. 1) for our study.

b. Satellite data

Infrared brightness temperature (IR_{BT}) data of geostationary satellites have been extensively used to study the life cycle characteristics of tropical MCSs (e.g., Mapes and Houze 1993; Machado et al. 1993; Chen and Houze 1997; Hodges and Thorncroft 1997; Gambheer and Bhat 2000; Roca and Ramanathan 2000; Mathon et al. 2002; Zuidema 2003; Kondo et al. 2006; Futyan and Del Genio 2007; Hennon et al. 2011; Fiolleau and Roca 2013; Berthet et al. 2017; Roca et al. 2017). We use 10.5–12.5-μm channel IR_{BT} data of *Kalpana-1*, an Indian geostationary satellite positioned at 74°E. The pixel size is 8 km × 8 km at the subsatellite point and the temporal resolution is 30 min. The study includes data of five monsoon seasons (July–August 2010, 2012–15).

For the objectives of this work, temporal continuity in data is very important. When this aspect was examined, imageries were found to be missing between 2230 and 0100 Indian standard time (IST) in the month of August that happens to be the ''satellite eclipse'' period of geostationary satellite positioned at 74°E. During the satellite eclipse period, satellite's solar panels do not see the sun and data are not collected owing to the lack of power. Except for this period, the fraction of missing imageries (including those removed after noticing noise during visual inspection) is about 7% with no preference to a particular time of a day, and temporal continuity in IR_{BT} data can be considered as good.

c. Large-scale dynamical fields

A synoptic-scale system is characterized by the large-scale low-level convergence that manifests as positive relative vorticity at the 850-hPa level (ζ_{850}) and divergence in the upper troposphere. The ζ_{850} and 700-hPa geopotential heights (Z_{700}) have been used to infer the synoptic-scale atmospheric forcing and the position of the monsoon trough, respectively (e.g., Gadgil 2003). These fields with 0.75° spatial and 6-hourly temporal resolution are taken from the ERA-Interim dataset (Dee et al. 2011). As far as Indian summer monsoon circulation is concerned, ERA data have a superior quality (Annamalai et al. 1999). Boos et al. (2015), Sørland and Sorteberg (2015), and Hunt et al. (2016b) have used ERA-Interim data to study the structure and dynamics of LPSs. ERA5 (ECMWF 2017) total column water vapor (TCWV) data with about 0.3° spatial and hourly temporal resolution are used for the moisture field. The smallest size of a CS over its lifespan can be 2000 km^2 (equivalent linear dimension ~45 km) and the minimum lifespan is 3 h. Therefore, ERA5 is chosen to study the link between moisture field and spatiotemporal evolution of a CS.

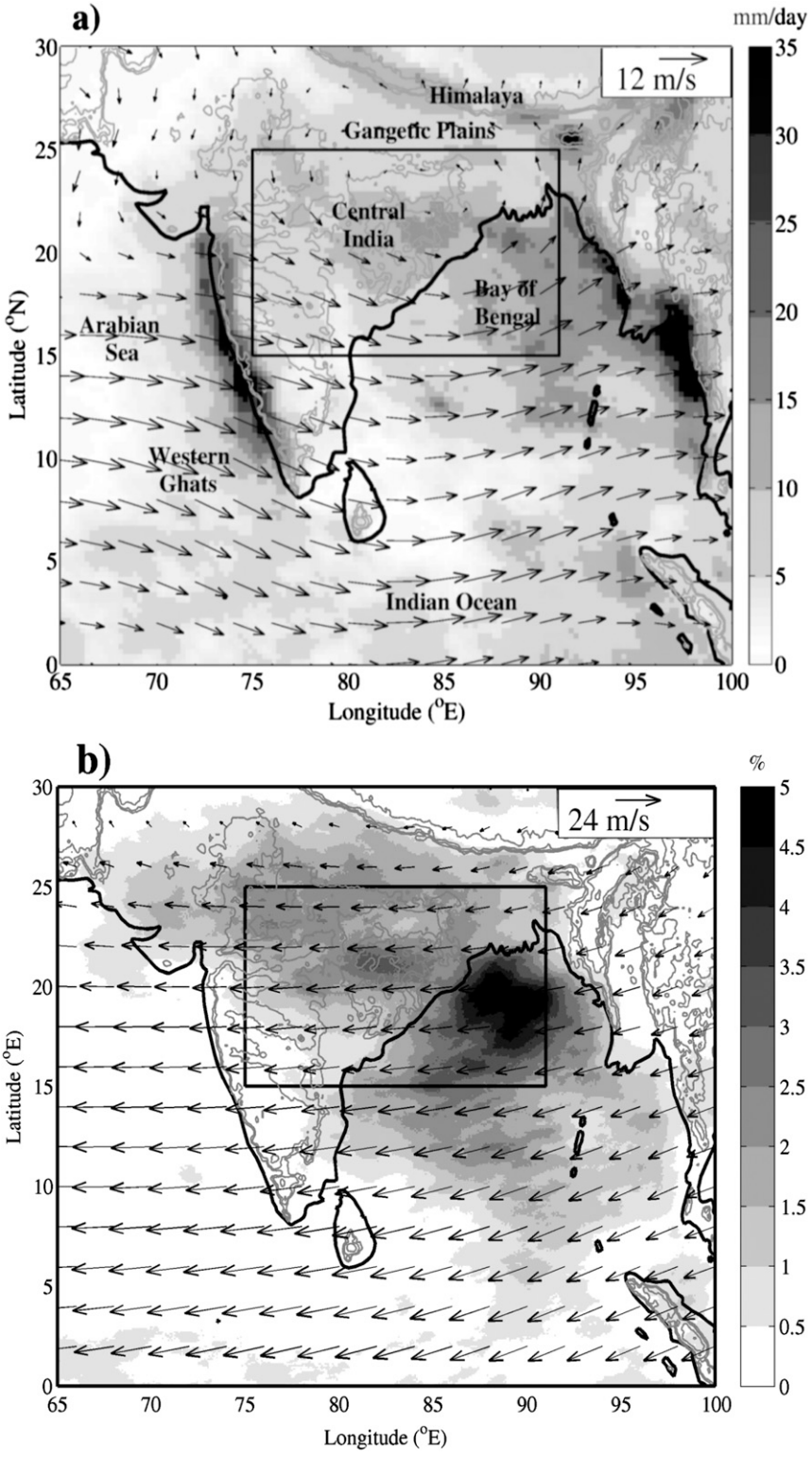

FIG. 1. (a) Climatology of TRMM 3B42 rainfall (Huffman et al. 2007) for July–August 2010–14 period and ERA-Interim 850-hPa winds for July–August 2010, 2012–15 period. (b) Fraction of the time infrared (10.5–12.5 μm) brightness temperature was 208 K or less during July–August 2010, 2012–15 and ERA-Interim 200-hPa winds. The rectangular box shows the study area.

The base state of the monsoon trough is produced by the land heating during the boreal summer [termed as heat low, e.g., Rao (1976)], and a positive low-level convergence and positive ζ_{850} are present over most parts of the study area throughout the summer monsoon season. The vertical circulation associated with the heat low is shallow and diverges around 700 hPa (Trenberth et al. 2000). When an LPS develops, ζ_{850} gets enhanced and the vertical circulation becomes deep. In the view of this, $\zeta_{850} > 0$ is a necessary but not a sufficient condition to infer the existence of synoptic-scale forcing over the monsoon zone. A threshold on ζ_{850} is needed to distinguish days with enhanced and suppressed synoptic-scale forcing. To decide the threshold, we examined the temporal variation of 3-day running average of positive ζ_{850} over the study area (henceforth denoted by $\overline{\zeta_{850}}$), the fraction of grids with positive ζ_{850} and $IR_{BT} < 235$ K, and IMD defined LPS periods over the region (Fig. 2). After studying data of all five seasons, a $\overline{\zeta_{850}}$ threshold of 2×10^{-5} s^{-1} ($\overline{\zeta_{t850}}$, henceforth) is adopted. Days with $\overline{\zeta_{850}} \geq \overline{\zeta_{t850}}$ fairly coincide with the days on which LPSs were present over the study region and an overall increase in the area under deep convection. Days with $\overline{\zeta_{850}} \geq \overline{\zeta_{t850}}$ are considered to be in the enhanced vorticity (EV) phase, and other days in the suppressed vorticity (SV) phase. Days with EV and SV are taken as strong and weak synoptic forcing periods, respectively. The total number of days that belong to the EV phase are 218 out of 310 days of July–August spread over 5 seasons (about 70% of the total). Normal position of the axis of the monsoon trough lies over the monsoon zone for about 74% of the time during July–August (Sikka and Gadgil 1980). Axis of the monsoon trough shifts to the foothills of the Himalayas during monsoon break conditions (e.g., Ramamurthy 1969). Thus, fraction of the days that belong to EV phase is nearly equal to the fraction of the days axis of the monsoon trough lies in its normal position. It may be noted that our definition of EV and SV phases is different from that of the monsoon ''active'' and ''break'' phases, which is traditionally based on the average daily rainfall either over entire India or the core monsoon zone (Rajeevan et al. 2010). SV phase approximately coincides with the monsoon break phase.

d. Automated cloud tracking

It is typical to specify a threshold on IR_{BT} to detect deep clouds and then search for connected pixels having their IR_{BT} less than or equal to the threshold to identify CSs (e.g., Williams and Houze 1987; Mapes and Houze 1993; Machado et al. 1993; Chen and Houze 1997; Hodges and Thorncroft 1997; Gambheer and Bhat 2000; Roca and Ramanathan 2000; Mathon et al. 2002; Zuidema 2003; Kondo et al. 2006; Futyan and Del Genio 2007; Hennon et al. 2011; Fiolleau and Roca 2013; Berthet et al. 2017; Roca et al. 2017). In this work, deep clouds are defined by an IR_{BT} threshold of 208 K, the same as that used by Williams and Houze (1987), Mapes and Houze (1993), Chen and Houze (1997), and Zuidema (2003). Hereafter, connected pixels having deep clouds and total area $\geq$2000 km^2 are called as ''objects.'' Objects are tracked in subsequent images to understand their temporal evolution. Overlap method is followed for tracking objects (Williams and Houze 1987). The minimum overlap required to locate a successor of an object in the next image is 25% of the area of smaller of the overlapping objects.

The IR_{BT} data used in the past cloud-tracking studies had 3-hourly temporal resolution, and there is ambiguity in uniquely identifying the successor at this temporal resolution (Roca et al. 2017). Main advantage of the 30-min temporal resolution is that relatively smaller objects can be tracked with high confidence and their life cycle can be studied from an early stage. An object that lived for at least 3 h and grew larger than 10^4 km^2 during its lifespan is called a cloud system (CS) in the following. No constraint on shape of the objects is put in defining CS. Location of a CS is the position of the center of gravity (CG) of the object area. Propagation speed of a CS is calculated by dividing the displacement of its CG in a given time interval. Examination of the propagation speeds based on 30-min time interval showed some abnormally high values. These occurred due to abrupt changes in the shapes of CSs that resulted in large displacement of the CGs. Propagation speed based on 1-h interval reduced the number of occurrences of such spikes, but some still remained. These cases are filtered out by applying the 3-sigma threshold criterion to the propagation speed distribution of each CS.

Propagation and lifetime characteristics of only those objects that qualified as CS are studied. Since 2230–0100 IST imageries are missing in August, this month's data are not included in the statistics of CSs lifetimes shown in the results. We did study the characteristics of CSs that formed in the month of August and observed that the CS lifespan histograms of July and August months are not very different from each other. The main reason is that the eclipse period of *Kalpana-1* satellite (i.e., midnight) happens to be the preferred time of dissipation of CSs over the study area.

3. Organization of deep convection over monsoon zone

Figures 3a and 3b show longitude–time diagrams of daily mean IR_{BT} averaged over the latitudinal belt

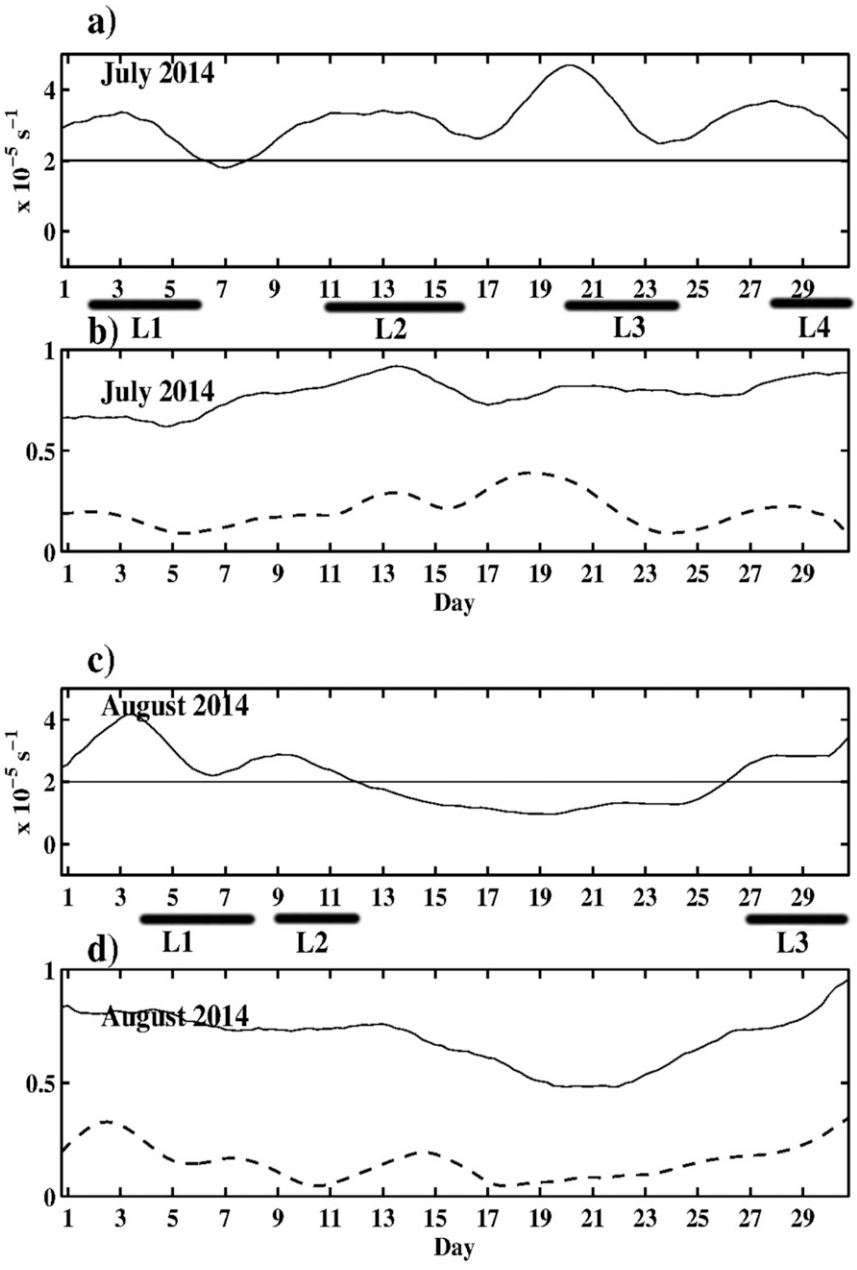

FIG. 2. 3-day running averages of: (a) $\overline{\zeta_{850}}$, (b) fraction of the area with cyclonic vorticity (solid line) and $IR_{BT} \leq 235$ K (dashed line) for July 2014 over the study box, and (c) as in (a) and (d) as in (b), but for August 2014. The letter "L" and the number following it refers to LPS and its number in that month. Thick horizontal lines show respective durations of LPSs over the study region given in the IMD monsoon report of 2014.

15°–25°N in July 2013 and 2014. Westward propagating envelops of large-scale cloudiness are observed westward of 85°E. These are mostly associated with the LPSs and last for 2–7 days. Figures 3c and 3d show zoomed-in views of two LPSs. Here, longitude–time diagrams are plotted with half-hourly IR_{BT} data. Starting time and tracks of CSs along with latitudinally averaged ζ_{850} are overlaid. Zooming on individual LPSs reveals that there is a diurnal modulation of deep convection, connected with the triggering, propagation and dissipation of CSs. Westward of 85°E (i.e., mainly over land), CSs develop in the afternoon hours preferentially in the western flank of ζ_{850} field where the gradient in ζ_{850} is high. Thereafter, CSs propagate westward and move

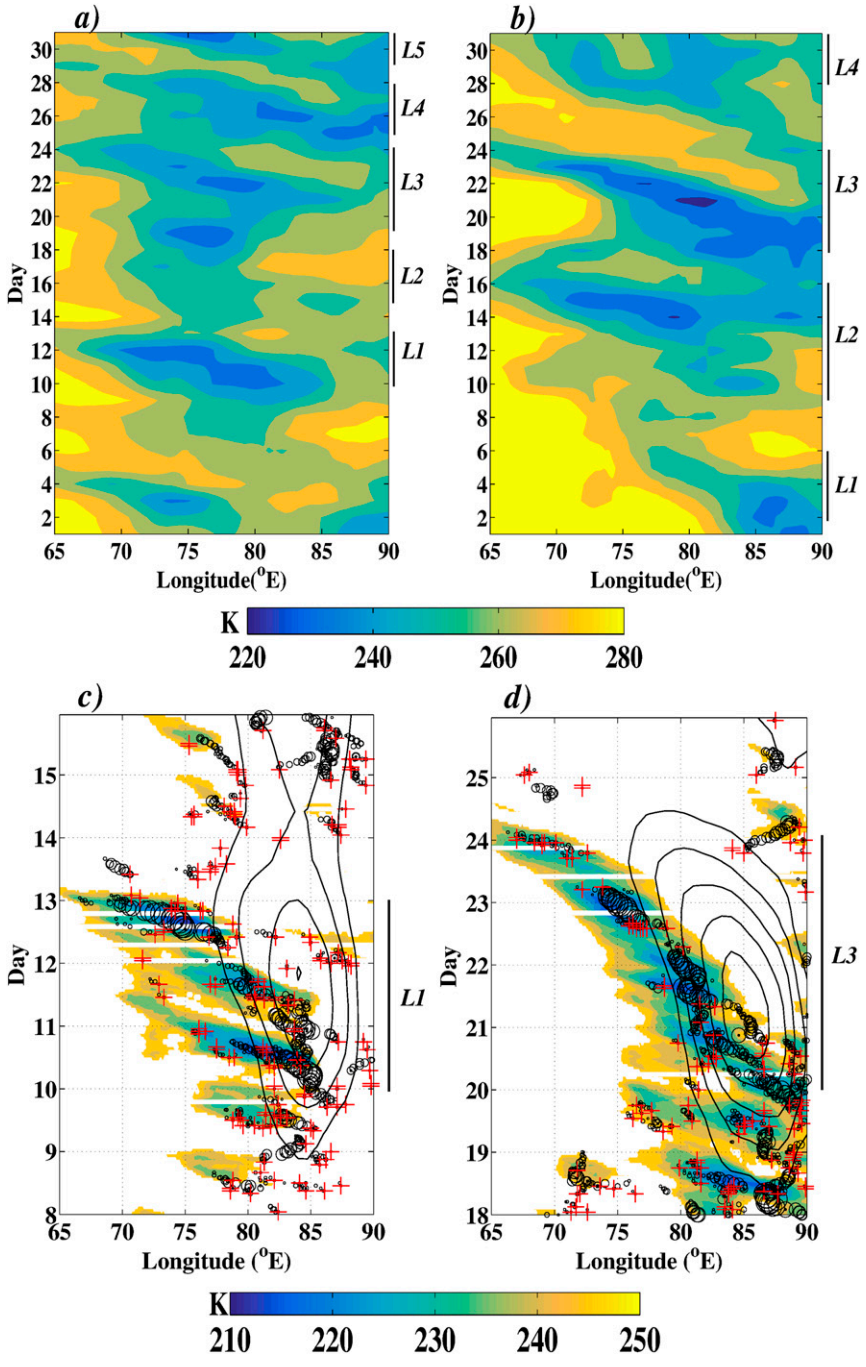

FIG. 3. Longitude–time Hovmöller diagram of IR_{BT} (in shading) averaged between 15° and 25°N for (a) July 2013, (b) July 2014, (c) zoomed-in view of (a), and (d) zoomed-in view of (b). In (a),(b) daily averaged IR_{BT} is shown. Note that the color bar scales are different in the top and bottom panels, with values of $IR_{BT} > 250$ K not shown in the latter. In (c),(d) object triggering (''+'' sign) and their subsequent positions (black circles) are overlaid on the Hovmöller diagram with radius of the circle proportional to the size of the object at that instant. The contour lines show relative vorticity at 850 hPa averaged over same latitudinal band. Contours from 2×10^{-5} to 4×10^{-5} s^{-1}, with an interval of 0.5×10^{-5} s^{-1} are plotted.

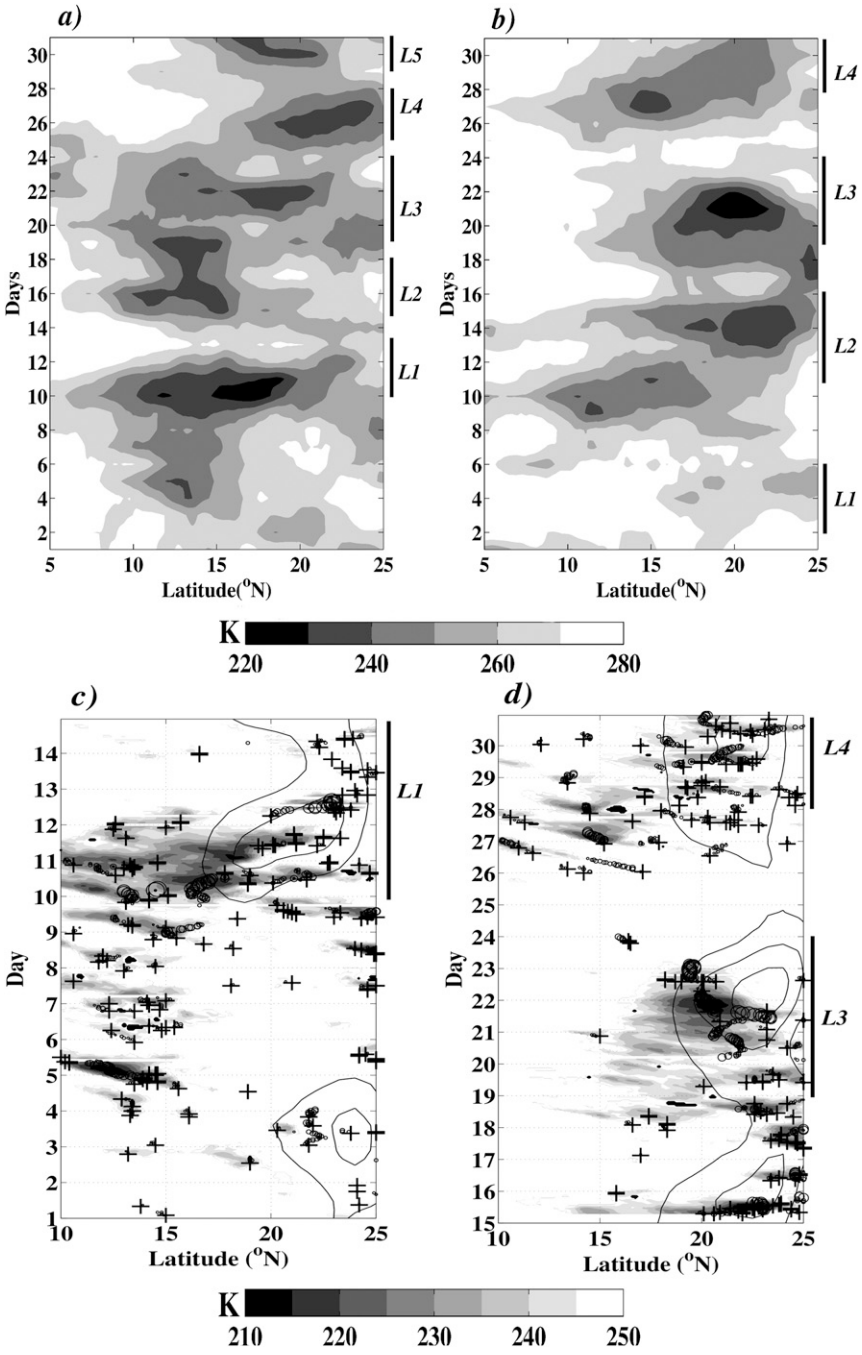

FIG. 4. Latitude–time Hovmöller diagram similar to Fig. 3; quantities are longitudinally averaged between 75° and 85°E.

out of the zone of high ζ_{850} region and dissipate around midnight when diurnal forcing becomes weak and surface conditions are less favorable for deep convection. Propagation of CSs is mainly zonal (westward) and meridional propagations are not that prominent (Fig. 4). Next day around midday, CSs develop in areas having large ζ_{850} gradient and around/behind the longitudes where the previous day's CSs had dissipated, and the cycle repeats. Each day, formations and westward propagations of CSs take the large-scale cloud envelop westward. Broadly, three types of propagations are embedded in Figs. 3c and 3d. First, deep cloud cover that spreads farther westward of CSs [which sometimes is called a "cloud streak," e.g., Carbone et al. (2002)].

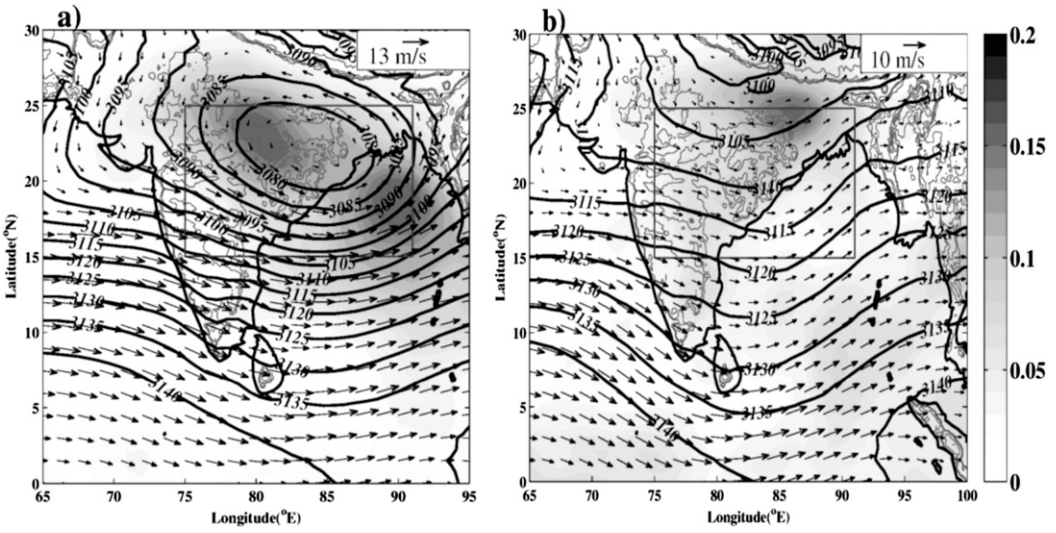

FIG. 5. Number of objects triggered per day during (a) EV and (b) SV phase over 1° × 1° spatial grid during July–August (in shading). Mean 850-hPa winds and 700-hPa geopotential contours during respectives phases are also overlaid.

Average speed of the streaks is around 20 m s^{-1}. Similar mesoscale streaks within the larger-scale convective envelopes are observed over the western Pacific and Maritime Continent (Nakazawa 1988; Mapes and Houze 1993; Chen and Houze 1997), over Africa (Laing et al. 2008), and over East Asia (Wang et al. 2004). Second, the CSs have a wider range of propagation speeds (details in the next section) with an average speed of 7.5 m s^{-1}. This discrepancy between speed of propagation of CS and cloud streak is due to the strong upper-level easterly jet that is invariably present during the monsoon season (Fig. 1b) that rapidly advects stratiform cloud mass westward. Third, the vorticity field which is associated with the synoptic system, propagates westward at a slower speed of around 2–3 m s^{-1}.

The morphology of timing and location of formation and subsequent propagation of CSs are broadly similar in all the cases of LPSs we have studied, not only during July–August but during the entire Indian summer monsoon season. The western flank of the low-level vorticity gradient is the breeding ground of CSs. CSs develop here in the afternoon hours when diurnal heating produces the most favorable conditions for convection over land. Once formed, CSs propagate well outside the area of formation and then dissipate. Formation of new CSs on the next day occurs in the wake of previous days CSs where vorticity gradient is present.

Figure 4 shows the latitude–time Hovmöller diagrams of IR_{BT}. A well organized southward propagation in a few cases is observed; the meridional propagations of CSs over Indian subcontinent, in general, is not as pronounced and as systematic as the zonal propagations. This point will again be highlighted in section 4c where CSs propagation statistics are presented. Several studies have reported southward propagating MCSs over the Bay (Zuidema 2003; Miyakawa and Satomura 2006; Liu et al. 2008; Sahany et al. 2010; Jain et al. 2018). We have observed southward propagating streaks over the Bay similar to these studies (not shown here). The southward propagation of deep convection over Bay is attributed to the diurnally generated coastal gravity waves (Mapes et al. 2003).

4. CSs characteristics and synoptic forcing

Figure 5 shows the spatial distribution of formation locations of objects during the EV and SV phases in July–August. Note that not all objects became CSs. The mean Z_{700} contours and 850-hPa winds show large-scale cyclonic circulation over monsoon zone during EV phase (Fig. 5a). During the SV phase, the cyclonic circulation is absent from the region (Fig. 5b). There are two preferred areas of formation of objects during EV phase, namely, north Bay and central India on the eastern and western flanks of the monsoon trough, respectively (Fig. 5a). The location over the Bay coincides with the location of maximum frequency of the genesis of LPSs and the northwest–southeast orientation of CS formation zone over central India lies along the tracks of LPSs (Sikka 1978; Goswami 2005; Krishnamurthy and Ajayamohan 2010; Hurley and Boos 2015; Hunt et al. 2016a). During the SV phase, triggering frequency is less and spread over a larger area with relatively more number of them occurring around 25°N, 85°E (i.e., closer to the foothills

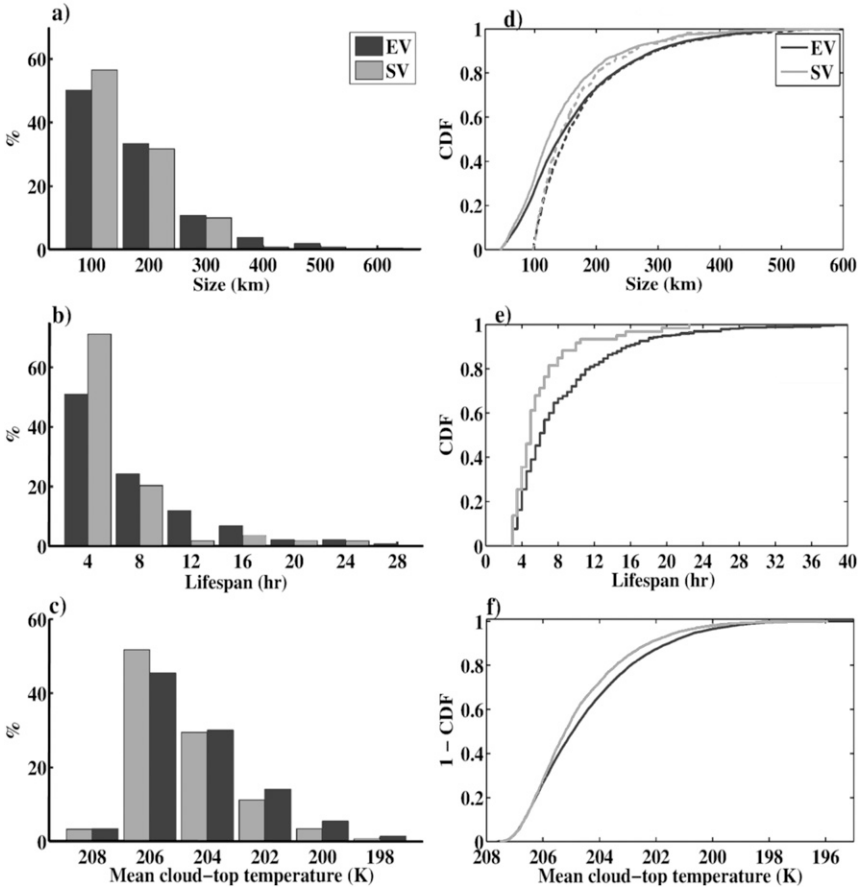

FIG. 6. Normalized histograms of (a) size of objects, (b) lifetime of CSs, and (c) mean cloud-top temperature of objects; and CDF of (d) size of objects, (e) lifetime of CSs, and (f) mean cloud-top temperature of objects. EV: enhanced vorticity, and SV: suppressed vorticity. The dotted lines in (d) show CDFs of maximum size of CSs.

of the Himalayas, and over the peninsular India as well). Note that the formation of objects is low over the heavily precipitating areas under the orographic influence (Western Ghats, Myanmar mountains, and eastern Himalaya foothills) during both EV and SV phases, further supporting the previous results that monsoon rainfall here is mainly from clouds that are not very deep and cloud tops that extend to 208 K height and meet the object's area criterion are less frequent (Arkin et al. 1989; Durai et al. 2010; Prakash et al. 2011).

a. Size, lifetime, and mean cloud-top temperature

Next we examine the contrasts in CSs properties between EV and SV phases over the monsoon zone. The total number of CSs that formed over the study area during the EV and SV phases in July–August (only July) are, respectively, 834 (531) and 213 (61). Figure 6a shows the size distribution of CSs formed over the monsoon zone during EV and SV phases. Here, all objects during the lifespan of CSs are considered (11 930 and 5455 respectively during EV and SV phases). Area of an object is converted to a linear scale by taking its square root. The size distribution of objects is well approximated by a lognormal distribution (not shown), in conformity with the previous studies (López 1977; Williams and Houze 1987; Mapes and Houze 1993). The fraction of objects with size less than 200 km is more during SV phase compared to EV phase, and the pattern is reversed for larger objects. Figure 6d shows the cumulative distribution functions (CDFs) of these size distributions (solid curves). The dotted curves show CDFs of maximum areas attained by CSs. It is observed that during the EV (SV) phase about 35% (25%) of CSs are larger than 200 km. The lifespan distributions (Fig. 6b) consider CSs formed only during July. Most of the CSs die within 24 h in both phases. The fraction of short-lived CSs in the SV phase is more compared to that in the EV phase. The CDFs in Fig. 6e show that during EV (SV) phase 30% (15%) of CSs live longer than 8 h. Figure 6c shows distributions of mean cloud-top temperature of

objects during the EV and SV phases. During the EV phase, mean cloud-top temperature tends to be lower than that during the SV phase (i.e., CSs are deeper during the EV phase). The CDFs (Fig. 6f) show that about 40% (30%) of convective objects have mean cloud-top temperature colder than 204 K during the EV phase. The two-sample Kolmogorov–Smirnov test performed on the CDFs of size, lifetime and cloud-top mean temperature during the EV and SV phases rejected the null hypothesis that the two samples are from the same distribution at 1% significance level. In summary, the probability of CSs being larger, longer lived, and deeper is higher during the EV phase. Since the study area includes both land and oceanic areas, it is possible that the characteristics of CSs over these two areas differ, and combining them is not ideal. To find this out, we repeated the analysis separately for the population of land and oceanic CSs. The outcome showed that the broad conclusions drawn from Fig. 6 hold good for the land and oceanic CSs also (Fig. S1 in the online supplemental material).

Figure 7 shows scatterplots of CSs maximum size versus lifetime (Fig. 7a) and object size versus mean cloud-top temperature (Fig. 7b). There is an approximate linear relationship between CSs size and lifespan during both phases. The correlation coefficient is 0.78 (0.89) during the EV (SV) phase. The longest lifespan of CS during the EV (SV) phase is about 38 (22) h. The largest size attained among all CSs is 639 km. The size of the largest CS formed over the Indian region is comparable to that over the TOGA COARE region of the western Pacific reported by Chen et al. (1996) at the same IR_{BT} threshold. There is a linear relationship between the object size and mean cloud-top temperature with a correlation coefficient of −0.8 during both phases. Thus, there exists a linear relationship between CSs size, lifespan, and cloud-top height regardless of the synoptic forcing. Previous studies have also observed a linear relationship between the CSs size and lifespan (Chen et al. 1996, Chen and Houze 1997, Roca et al. 2017), and CSs size and cloud-top height (Machado et al. 1992, Roca and Ramanathan 2000) in tropical CSs. These studies did not classify the CSs population according the regime of large-scale conditions in which they were formed. The correlation coefficient between CSs maximum size and lifetime reported by Roca et al. (2017) is similar to that found in this study, although they used 235 K (i.e., a much higher IR_{BT} threshold).

b. Diurnal variation

Figures 8a and 8b show diurnal variation of the first detection time (formation, henceforth) of the objects over the Indian landmass (18°–25°N, 75°–85°E) and over the Bay area (15°–20°N, 85°–91°E), respectively, during

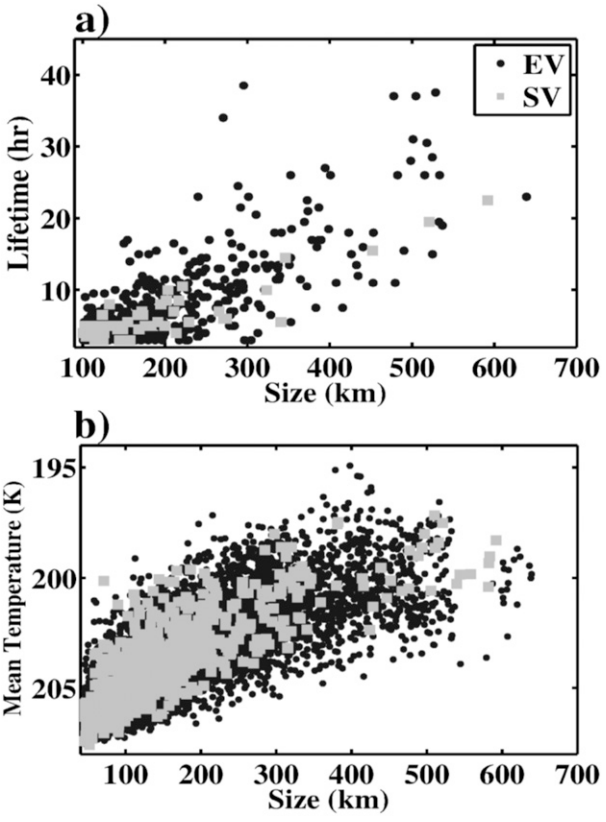

FIG. 7. (a) Maximum size vs lifespan of CSs. (b) Size vs mean cloud-top temperature of objects. EV: enhanced vorticity, and SV: suppressed vorticity.

the EV and SV phases. Over land, irrespective of the phase, object formation peaks during 1500–1800 LST and the least preferred time is around 0900 LST. Over the Bay, two peaks are observed in the diurnal variation of objects triggering during the SV phase. The major peak is around 1200 LST and the minor peak is around 0300 LST (Fig. 8b). The nocturnal triggering of convection mainly occurs near to the coast (not shown). During the EV phase, a clear secondary nocturnal peak over the Bay is not seen.

For the land box, Fig. 8c shows diurnal variation of formation of CSs. When a CS splits, the larger sized CS of the two is taken as continuation of the parent CS and the other is treated as a new one. To understand the contribution of splits to the statistics of CS formation time, two cases are shown in Fig. 8c for the land region. The dashed line includes all the CSs (i.e., including those formed out of splits) and the solid line includes only those CSs which did not form by split. Diurnal variation of CSs formation is more pronounced compared to that of the objects with a clear preference to ~1500 LST during both EV and SV phases. Those born out of CS splitting make only a marginal changes to this.

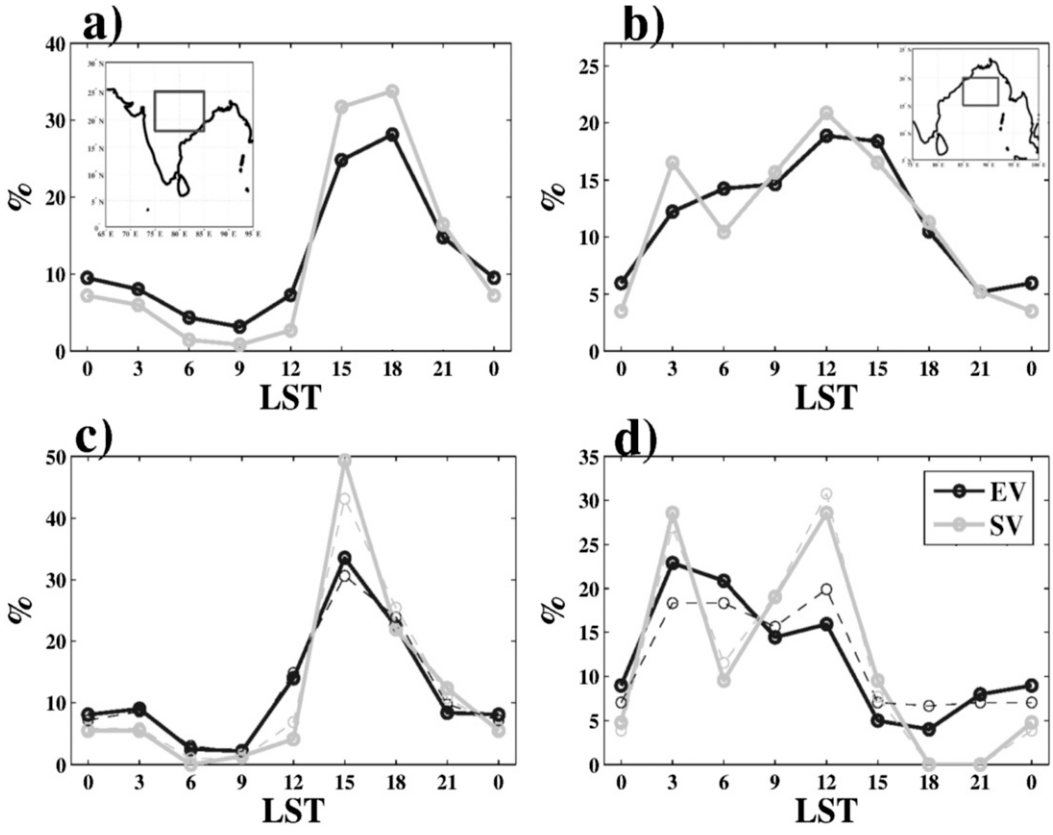

FIG. 8. Diurnal variation of objects triggering over (a) land, 18°–25°N, 75°–85°E (total 1851 during EV and 521 during SV), and (b) Bay, 15°–20°N, 85°–91°E, (total 1101 during EV and 119 during SV). These regions are shown by the boxes in the insets. (c) Dashed and solid lines correspond to diurnal variation of formation of all the CSs (total 397 during EV and 92 during SV) and only those CSs that did not form by splitting (total 348 during EV and 77 during SV), respectively, over land. (d) As in (c), but for the Bay region. Number of CSs formed over Bay without splitting during EV and SV phases are 219 and 22, respectively. The corresponding total number of all CSs formations are 274 and 27.

Figure 8d shows the diurnal variation of CSs over the Bay box. A clear difference in the diurnal variation of objects and CSs is seen in the EV phase with a clear preference of CSs formation to the early morning (~0300 LST) hours, and the 1200–1500 LST peak has subsided. During the SV phase, both early morning and noon hours have comparable preference and ~1800 LST is the least preferred time.

c. *Propagation*

Figure 9 shows the distributions of zonal and meridional speeds of CSs in the EV and SV phases. The propagation speeds of about 95% of CSs are less than $20\,m\,s^{-1}$. Figure 9a shows that regardless of the synoptic forcing, the majority of the CSs propagate westward. Eastward propagations are not only lesser in number but also slower than the westward propagations. The mean speed of all westward propagations is about $8.5\,m\,s^{-1}$ and that of eastward propagations is about $4.5\,m\,s^{-1}$. Although, the zonal propagation speed distribution during EV and SV phases look similar, the two-sample Kolmogorov–Smirnov test rejected the null hypothesis that the two samples are from the same continuous distribution at 1% significance level. The westward propagations of CSs are faster during the SV phase (mean speed = $9.5\,m\,s^{-1}$) than the EV phase (mean speed = $7.5\,m\,s^{-1}$). The meridional propagation speed distribution (Fig. 9b) of CSs is centered around $0\,m\,s^{-1}$; speeds greater than $10\,m\,s^{-1}$ are rare. Southward propagations are favored over northward propagations during the EV phase.

d. *The broad picture*

In the statistical analysis, individuality of CSs is lost. Their large number makes it difficult to carry out a detailed analysis of individual cases. It is observed from Fig. 6a that the number of objects having size ≥ 300 km is relatively small and study of their life cycle can be attempted. Here, a CS with its peak size ≥ 300 km is

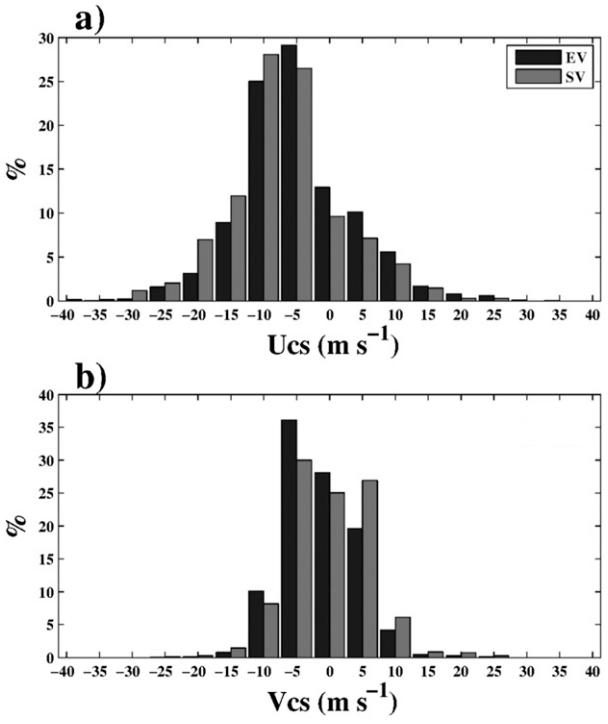

FIG. 9. Distribution of CSs propagation velocity. (a) Zonal component and (b) meridional component.

called as "large CS." Figures 10a and 10b show where the large CSs were triggered and achieved their maximum size, respectively. During the EV phase, large CSs get triggered mainly over the monsoon zone. A stretch on either of the east coast of India is one of the favorable locations of formation of large CSs, and then they propagate away from the coast. Over land, they predominantly propagate westward and achieve their largest size after traveling several hundred kilometers (Fig. 10b). As a consequence, more number of large CSs are observed over the western part of India compared to the eastern part during the EV phase. Over the Bay, large CSs tend to propagate away from coast and achieve maximum size over the open Bay. The northward propagations of CSs are rare here. This observation is in agreement with Zuidema (2003) and Miyakawa and Satomura (2006).

The sizes of large CSs are comparable to those over the Bay and land during the EV phase. During the SV phase, largest of the CSs are triggered over the Gangetic plains. CSs triggered near to the foothills of the Himalayas tend to propagate southward while those over plains propagate westward. CSs achieve their maximum area over Gangetic plains and somewhat to the south of it during the SV phase. During this phase, the maximum areal extent of CSs over Bay rarely reached 400 km. Thus, the large CSs that form the tail of the size distribution in the SV phase (Fig. 6a) occur only over the parts of Gangetic plains sampled in the study box. Large CSs form over the equatorial Indian Ocean and south Bay only during the SV phase.

5. Discussion

One question that arises from Figs. 3c and 3d is why CSs form in the western flank of the vorticity gradient field? Within the planetary boundary layer (PBL), there is convergence (divergence) when circulation is cyclonic (anticyclonic) according to Ekman theory and the vertical velocity at the top of PBL is related to the geostrophic vorticity above PBL by the following equation (Holton and Hakim 2012a):

$$w(\mathrm{De}) = \zeta_g = \left|\frac{K_m}{2f}\right|^{1/2}\left(\frac{f}{|f|}\right), \tag{1}$$

where $w(\mathrm{De})$ and ζ_g are the vertical velocity and the vertical component of relative vorticity, respectively, at height D_e from the surface (the top of the Ekman layer); K_m is eddy viscosity; and f is Coriolis parameter. This equation suggests a symmetry in the rising motion within a barotropic cyclonic vortex (Charney and Eliassen 1964). Along the monsoon trough, horizontal temperature gradients cannot be ignored, and the barotropic assumption made in deriving Eq. (1) is not valid. The other theory used for explaining vertical velocity in more complex situations is the quasigeostrophic (QG) theory, according to which in a vertically sheared environment low-level ascent is induced in the down-shear portion of the vortex (e.g., Raymond (1992); Jones (1995); Frank and Ritchie (2001). Following Boos et al. (2015), the isobaric form of QG omega equation over a β plane can be written as

$$\left(\sigma\nabla^2 + f_o^2\frac{\partial^2}{\partial p^2}\right)\omega = -2\nabla\cdot\mathbf{Q} - \frac{R}{p}\beta\frac{\partial T}{\partial x}, \tag{2}$$

where ω is the vertical velocity in pressure coordinate, $\sigma = \rho^{-1}\partial_p \ln\theta$ the static stability of atmosphere, β is the meridional gradient of Coriolis parameter, f_o is the mean Coriolis parameter, T is temperature, p is pressure, R is the gas constant, and $\mathbf{Q}$ is a vector containing horizontal derivatives of horizontal velocity and temperature [chapter 6 of Holton and Hakim (2012b)]. This form was originally given by Hoskins et al. (1978) over an f plane. The term of $\nabla\cdot\mathbf{Q}$ can be expressed as (Kiladis et al. 2006)

$$\frac{P}{R}\nabla\cdot\mathbf{Q} = \frac{\partial T}{\partial x}\frac{\partial \zeta}{\partial y} - \frac{\partial T}{\partial y}\frac{\partial \zeta}{\partial x} + \frac{\partial^2\psi}{\partial x\partial y}\left(\frac{\partial^2 T}{\partial x^2} - \frac{\partial^2 T}{\partial y^2}\right) - \frac{\partial^2 T}{\partial x\partial y}\left(\frac{\partial^2\psi}{\partial x^2} - \frac{\partial^2\psi}{\partial y^2}\right), \tag{3}$$

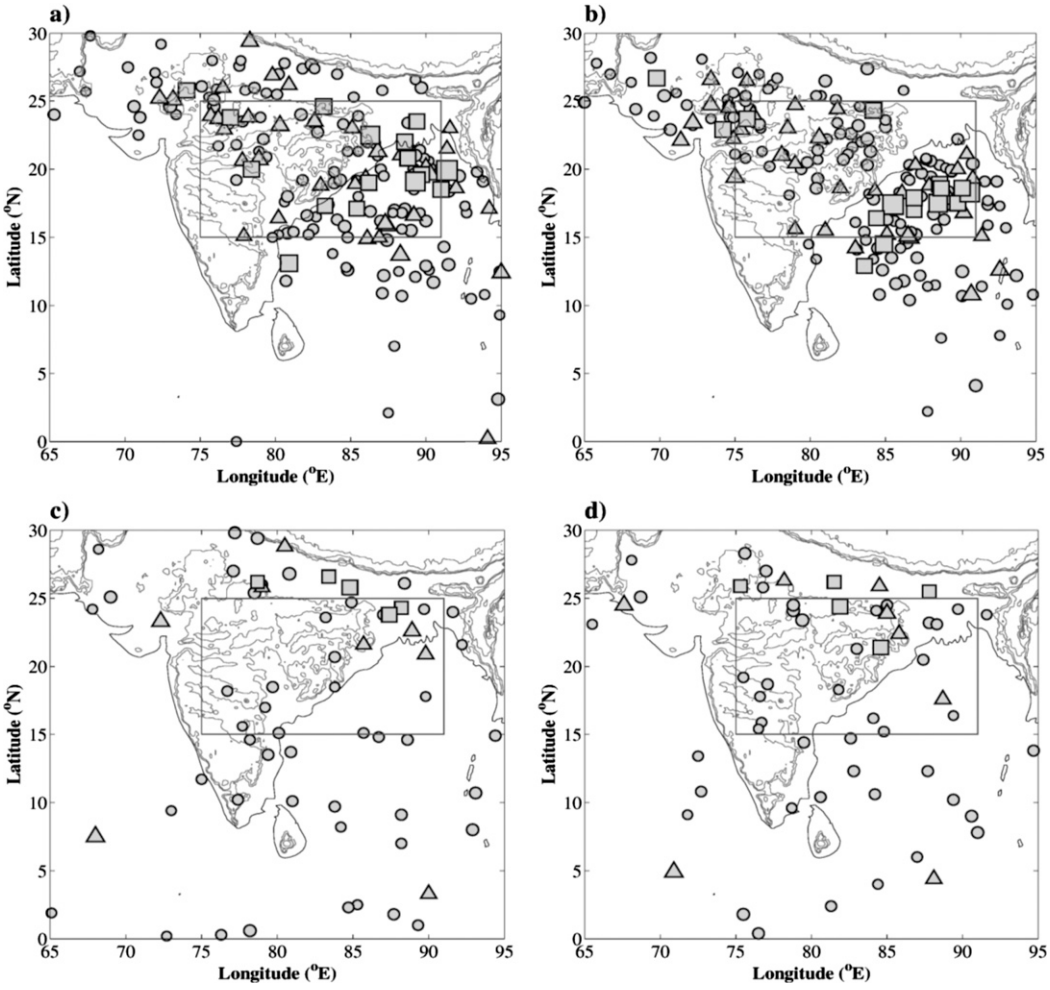

FIG. 10. Spatial distribution of (a) formation and (b) peak in the size of large CSs during the EV phase. (c) As in (a) and (d) as in (b), but during the SV phase. The size of a symbol is made proportional to the peak area of the CS. Different types of symbols refer to different size categories—1) ●: 300 ≤ size < 400 km, 2) ▲: 400 ≤ size < 500 km, and 3) ■: size ≥ 500 km.

where ψ is the streamfunction of the horizontal wind taken as, $\psi = gZ/f_o$, where Z is geopotential height (Sanders 1984). Right-hand side (rhs) of Eq. (2) gives the synoptic forcing on ω which we calculated using the ERA-Interim data.

Figures 11a and 11c show vertical velocity and relative vorticity fields at 850 hPa on one day during the lifetimes of LPSs shown in the Figs. 3c and 3d, respectively. Corresponding QG forcing calculated from the rhs of Eqs. (2) and (3) is shown in Figs. 11b and 11d. Positions of CSs are overlaid in both figures. Stronger ascending motion is observed at 850 hPa at two locations—one in the west-southwest sector of the LPSs where the QG forcing is positive, and the other along the west coast of India. The latter is normally attributed to orographic lifting. QG forcing is dominant in the west-southwest sector of LPSs and weak over the west coast of India. Larger CSs formed preferably in the region having high QG forcing. The ascending motion is suppressed in the northeast sector of LPSs where the QG forcing is negative. Formation of CSs is also seen on the eastern side of LPS over the head Bay (Figs. 11c,d). However, the CSs formed on the western side are the ones that grow larger in size and last longer. Broad features observed in Fig. 11 are similar during other EV events as well (Fig. S2 shows cases of three more EV events).

In a recent study, Adames and Ming (2018b) showed that the advection of dry static energy by the large-scale circulation of LPS promotes larger clouds on its western side. They also show that the convective heating term associated with the clouds contributes predominantly to the total ascent on the western side of the LPS; the ascent also maintains the moisture anomalies of the LPS. It is observed from Figs. 3c and 3d that there is some

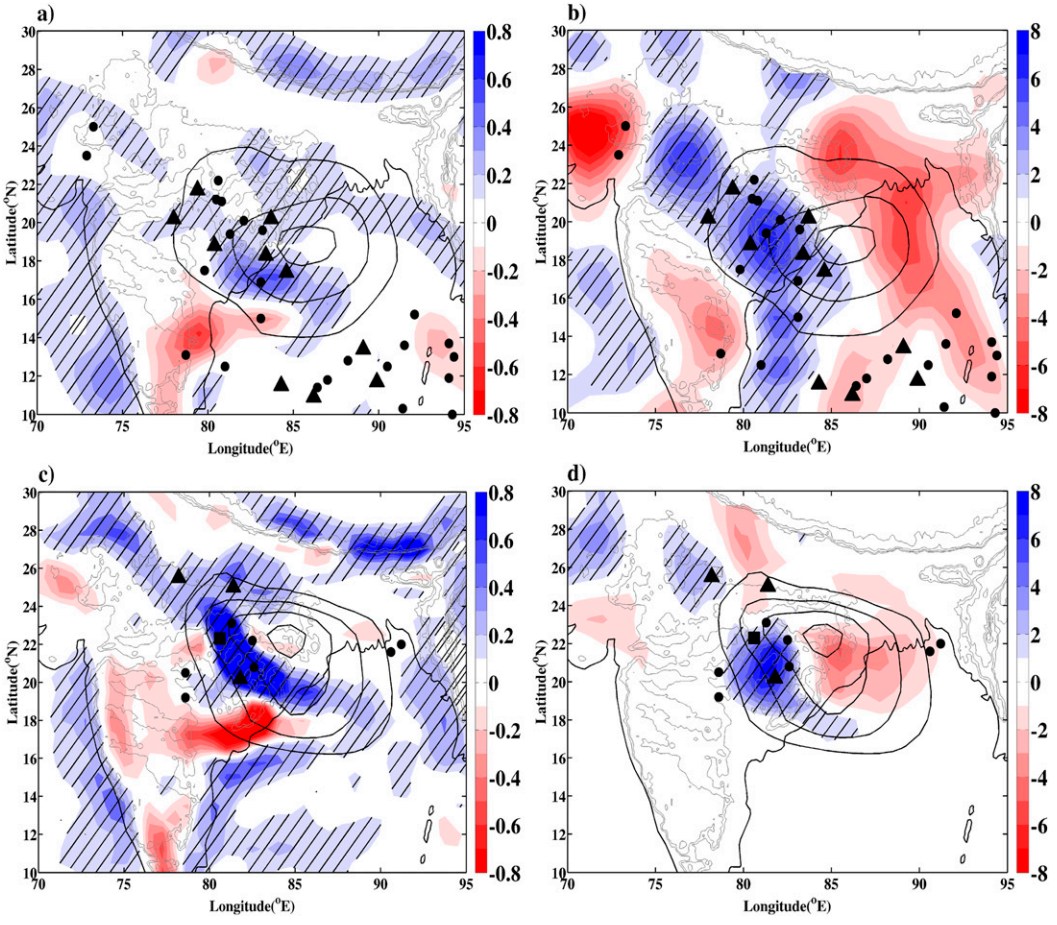

FIG. 11. (a) Vertical velocity ($\mathrm{Pa\,s^{-1}}$) at 850 hPa from ERA-Interim data, (b) quasigeostrophic forcing ($\times 10^{-15}\,\mathrm{Pa^{-1}\,s^{-3}}$) at 850 hPa calculated from Eqs. (2) and (3) using ERA-Interim data. Both fields are shown at 1200 UTC 11 Jul 2013. (c) As in (a), (d) as in (b), but at 1200 UTC 21 Jul 2014. Contours show ζ_{850} field with values starting from $2 \times 10^{-15}\,\mathrm{s^{-1}}$ with a contour interval of $2 \times 10^{-15}\,\mathrm{s^{-1}}$. Black symbols show locations of CSs and smaller tracked objects formed on respective days. Different types of symbols refer to different peak size categories – 1) ●: 50 ≤ size < 100 km (not classified as CS), 2) ▲: 100 ≤ size < 300 km, and 3) ■: size ≥ 300 km.

preference for the CSs to form in the neighborhood where CSs of the previous day had dissipated. Adames and Ming (2018a) with the help of linearized primitive equations showed that the intensification of LPS is possible only when the moistening is ahead of the LPS. To examine this possibility in the monsoonal LPSs, we plotted the total column water vapor (TCWV) anomaly field from the ERA5 dataset for the LPS cases shown in Figs. 3c and 3d (Fig. 12). The triggering and dissipation locations of CSs are also shown. It is observed from Fig. 12 that the moisture anomalies propagate with the CSs and ahead of the synoptic system. New CSs form next day in areas with positive moisture anomaly. Figure S3 shows four more EV cases similar to Fig. 12.

The preference for the westward propagation by the tropical MCSs is a globally observed phenomenon (Tulich and Kiladis 2012; Dias et al. 2017) and this preference is seen here in the Indian monsoonal CSs over land during both EV and SV phases. Triggering and propagation of CSs are two independent aspects; the former is influenced by synoptic forcing and orography, and the latter is governed by the large-scale wind field and MCS dynamics, in particular, by the convectively generated gravity waves and cold pools (Cotton et al. 2010a). Vertical shear of winds can force the gravity waves to propagate westward (Stechmann and Majda 2009). Tulich and Kiladis (2012) explain the westward propagation of MCSs by linking it to the westward propagating inertial-gravity waves modulated by the low-level vertical wind shear. During the Indian summer monsoon season, vertical shear in the zonal winds is omnipresent although its strength may differ between the EV and SV phases (Fig. 13b). Meridional winds are comparatively weaker over the land region (Fig. 13c)

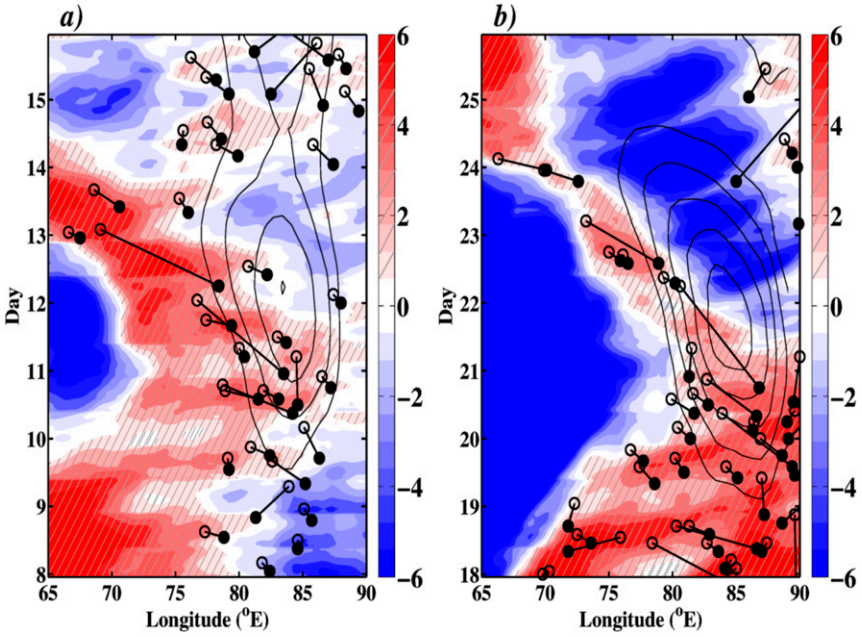

FIG. 12. Longitude–time Hovmöller diagram of ERA5 total column water vapor (TCWV) field (kg m^{-2}) in shading, averaged between 15° and 25°N for (a) July 2013 and (b) July 2014. The filled and open circles show the triggering and dissipation locations, respectively, of CSs as per the tracking algorithm.

and may not affect CS propagation. It is plausible that the westward propagation of monsoonal CSs are coupled to the convectively generated gravity waves. Convergence caused by the cold pools on the upwind side of the MCSs is also a possibility (e.g., Rotunno et al. 1988). The midtroposphere is drier during the SV phase compared to the EV phase (Fig. 13a). The differences below 800 hPa are less between the two phases, and owing to this, the downdrafts driven by the evaporative cooling of falling raindrops (Cotton et al. 2010b) may not be very different, and hence no major difference in the propagation characteristics of the two phases is expected.

6. Conclusions

Modulation of properties of CSs by the synoptic forcing during Indian summer monsoon season is studied using the *Kalpana-1* satellite data and a tracking algorithm. The 850-hPa vorticity field is used as a proxy

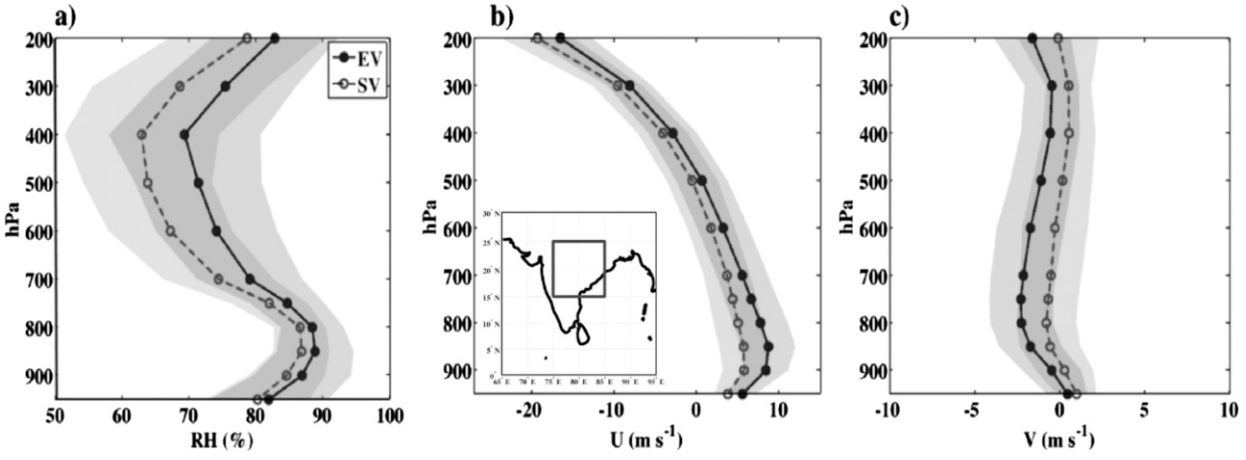

FIG. 13. Mean vertical profiles of ERA-Interim (a) relative humidity (RH), (b) zonal winds (U), and (c) meridional winds (V) averaged over 15°–25°N, 75°–85°E [region shown by the box in (b) during EV and SV phase]. The shading shows one standard deviation.

for the synoptic-scale forcing. Following conclusions are drawn from this study:

1) There is a systematic organization of CSs within the LPSs. Large, long-lasting CSs predominantly form on the western side of LPSs in the region of ζ_{850} gradient and propagate farther westward with a mean speed of 7.5 m s^{-1}. CSs propagation over the Indian land is mainly zonal during both EV and SV phases, implying that the westward propagation of CSs is not particularly associated with the synoptic vorticity filed.
2) EV phase promotes formation of larger, deeper, and longer-lived CSs over the monsoon zone. During the SV phase, large CSs form over the Gangetic plains. Their sizes are comparable to those formed over monsoon zone during the EV phase. Irrespective of the phase of the large-scale forcing, there is a linear relationship between CSs size, lifespan, and mean cloud-top temperature.
3) During the EV phase, triggering of CSs mainly occurs over a northwest–southeast-oriented narrow corridor of monsoon zone. This corridor is connected by two maxima, one over the north Bay and the other over central India; and it coincides with the climatological passage of propagation of synoptic systems. During the SV phase, the triggering is more widespread over the region and it is predominantly tied to the orographic features.
4) The diurnal variation of CSs formation is more pronounced during the SV phase than the EV phase over Indian land and Bay. Over land, there is a sharp peak at 1500 LST irrespective of the synoptic forcing. Over the Bay, during SV phase two peaks are seen, one at 0300 LST and the other at 1200 LST, whereas, during the EV phase, CSs formation mainly occurs in the nocturnal hours; these CSs grow subsequently and split during the daytime forming more number of smaller CSs over the Bay.

Acknowledgments. Data for 2010, 2014–15 seasons were downloaded from the Meteorological and Oceanographic Satellite Data Archival Centre (MOSDAC), Space Application Centre, Indian Space and Research Organization (ISRO) and for 2012–13, data were obtained from the India Meteorological Department (IMD) through the Continental Tropical Convergence Zone (CTCZ) program. The authors thank IMD, MOSDAC, the Ministry of Earth Sciences, the CTCZ program, ECMWF for the ERA-Interim data, and NASA for the TRMM data.

REFERENCES

Adames, Á. F., and Y. Ming, 2018a: Interactions between water vapor and potential vorticity in synoptic-scale monsoonal disturbances: Moisture vortex instability. *J. Atmos. Sci.*, **75**, 2083–2106, https://doi.org/10.1175/JAS-D-17-0310.1.

——, and ——, 2018b: Moisture and moist static energy budgets of South Asian monsoon low pressure systems in GFDL AM4.0. *J. Atmos. Sci.*, **75**, 2107–2123, https://doi.org/10.1175/JAS-D-17-0309.1.

Annamalai, H., J. Slingo, K. Sperber, and K. Hodges, 1999: The mean evolution and variability of the Asian summer monsoon: Comparison of ECMWF and NCEP–NCAR reanalyses. *Mon. Wea. Rev.*, **127**, 1157–1186, https://doi.org/10.1175/1520-0493(1999)127<1157:TMEAVO>2.0.CO;2.

Arkin, P. A., A. Krishna Rao, and R. Kelkar, 1989: Large-scale precipitation and outgoing longwave radiation from INSAT-1B during the 1986 southwest monsoon season. *J. Climate*, **2**, 619–628, https://doi.org/10.1175/1520-0442(1989)002<0619:LSPAOL>2.0.CO;2.

Berthet, S., R. Roca, J. Duvel, and T. Fiolleau, 2017: Subseasonal variability of mesoscale convective systems over the tropical northeastern Pacific. *Quart. J. Roy. Meteor. Soc.*, **143**, 1086–1094, https://doi.org/10.1002/qj.2992.

Boos, W., J. Hurley, and V. Murthy, 2015: Adiabatic westward drift of Indian monsoon depressions. *Quart. J. Roy. Meteor. Soc.*, **141**, 1035–1048, https://doi.org/10.1002/qj.2454.

Carbone, R., J. Tuttle, D. Ahijevych, and S. Trier, 2002: Inferences of predictability associated with warm season precipitation episodes. *J. Atmos. Sci.*, **59**, 2033–2056, https://doi.org/10.1175/1520-0469(2002)059<2033:IOPAWW>2.0.CO;2.

Charney, J. G., and A. Eliassen, 1964: On the growth of the hurricane depression. *J. Atmos. Sci.*, **21**, 68–75, https://doi.org/10.1175/1520-0469(1964)021<0068:OTGOTH>2.0.CO;2.

Chen, S. S., and R. A. Houze, 1997: Diurnal variation and life-cycle of deep convective systems over the tropical Pacific warm pool. *Quart. J. Roy. Meteor. Soc.*, **123**, 357–388, https://doi.org/10.1002/qj.49712353806.

——, ——, and B. E. Mapes, 1996: Multiscale variability of deep convection in realation to large-scale circulation in TOGA COARE. *J. Atmos. Sci.*, **53**, 1380–1409, https://doi.org/10.1175/1520-0469(1996)053<1380:MVODCI>2.0.CO;2.

Cotton, W. R., G. Bryan, and S. C. Van den Heever, 2010a: Cumulonimbus clouds and severe convective storm. *Storm and Cloud Dynamics*, 2nd ed. Academic Press, 315–428.

——, ——, and ——, 2010b: Mesoscale convective systems. *Storm and Cloud Dynamics*, 2nd ed. Academic Press, 455–526.

Dee, D. P., and Coauthors, 2011: The ERA-Interim reanalysis: Configuration and performance of the data assimilation system. *Quart. J. Roy. Meteor. Soc.*, **137**, 553–597, https://doi.org/10.1002/qj.828.

Dias, J., N. Sakaeda, G. N. Kiladis, and K. Kikuchi, 2017: Influences of the MJO on the space-time organization of tropical convection. *J. Geophys. Res. Atmos.*, **122**, 8012–8032, https://doi.org/10.1002/2017JD026526.

Durai, V., S. Bhowmik, and B. Mukhopadhyay, 2010: Evaluation of Indian summer monsoon rainfall features using TRMM and KALPANA-1 satellite derived precipitation and rain gauge observation. *Mausam*, **61**, 317–336.

ECMWF, 2017: ERA5: Fifth generation of ECMWF atmospheric reanalyses of the global climate. Copernicus Climate Change Service Climate Data Store (CDS), accessed 3 January 2019, https://confluence.ecmwf.int/display/CKB/ERA5+data+documentation.

Fiolleau, T., and R. Roca, 2013: Composite life cycle of tropical mesoscale convective systems from geostationary and low earth orbit satellite observations: Method and sampling considerations. *Quart. J. Roy. Meteor. Soc.*, **139**, 941–953, https://doi.org/10.1002/qj.2174.

Frank, W. M., and E. A. Ritchie, 2001: Effects of vertical wind shear on the intensity and structure of numerically simulated hurricanes. *Mon. Wea. Rev.*, **129**, 2249–2269, https://doi.org/10.1175/1520-0493(2001)129<2249:EOVWSO>2.0.CO;2.

Futyan, J. M., and A. D. Del Genio, 2007: Deep convective system evolution over Africa and the tropical Atlantic. *J. Climate*, **20**, 5041–5060, https://doi.org/10.1175/JCLI4297.1.

Gadgil, S., 2003: The Indian monsoon and its variability. *Annu. Rev. Earth Planet. Sci.*, **31**, 429–467, https://doi.org/10.1146/annurev.earth.31.100901.141251.

Gambheer, A. V., and G. Bhat, 2000: Life cycle characteristics of deep cloud systems over the Indian region using INSAT-1B pixel data. *Mon. Wea. Rev.*, **128**, 4071–4083, https://doi.org/10.1175/1520-0493(2000)129<4071:LCCODC>2.0.CO;2.

Goswami, B., 2005: South Asian monsoon. *Intraseasonal Variability in the Atmosphere-Ocean Climate System*, W. K.-M. Lau and D. E. Waliser, Eds., Springer, 19–61.

Hennon, C. C., C. N. Helms, K. R. Knapp, and A. R. Bowen, 2011: An objective algorithm for detecting and tracking tropical cloud clusters: Implications for tropical cyclogenesis prediction. *J. Atmos. Oceanic Technol.*, **28**, 1007–1018, https://doi.org/10.1175/2010JTECHA1522.1.

Hodges, K. I., and C. Thorncroft, 1997: Distribution and statistics of African mesoscale convective weather systems based on the ISCCP Meteosat imagery. *Mon. Wea. Rev.*, **125**, 2821–2837, https://doi.org/10.1175/1520-0493(1997)125<2821:DASOAM>2.0.CO;2.

Holton, J. R., and G. J. Hakim, Eds., 2012a: The planetary boundary layer. *An Introduction to Dynamic Meteorology*, 5th ed. Academic Press, 256–276.

——, and ——, 2012b: Quas-geostrophic analysis. *An Introduction to Dynamic Meteorology*, 5th ed. Academic Press, 171–210.

Hoskins, B., I. Draghici, and H. Davies, 1978: A new look at the ω-equation. *Quart. J. Roy. Meteor. Soc.*, **104**, 31–38, https://doi.org/10.1002/qj.49710443903.

Houze, R. A., 1989: Observed structure of mesoscale convective systems and implications for large-scale heating. *Quart. J. Roy. Meteor. Soc.*, **115**, 425–461, https://doi.org/10.1002/qj.49711548702.

——, 2004: Mesoscale convective systems. *Rev. Geophys.*, **42**, RG4003, https://doi.org/10.1029/2004RG000150.

Huffman, G. J., and Coauthors, 2007: The TRMM Multisatellite Precipitation Analysis (TMPA): Quasi-global, multiyear, combined-sensor precipitation estimates at fine scales. *J. Hydrometeor.*, **8**, 38–55, https://doi.org/10.1175/JHM560.1.

Hunt, K. M., A. G. Turner, P. M. Inness, D. E. Parker, and R. C. Levine, 2016a: On the structure and dynamics of Indian monsoon depressions. *Mon. Wea. Rev.*, **144**, 3391–3416, https://doi.org/10.1175/MWR-D-15-0138.1.

——, ——, and D. E. Parker, 2016b: The spatiotemporal structure of precipitation in Indian monsoon depressions. *Quart. J. Roy. Meteor. Soc.*, **142**, 3195–3210, https://doi.org/10.1002/qj.2901.

Hurley, J. V., and W. R. Boos, 2015: A global climatology of monsoon low-pressure systems. *Quart. J. Roy. Meteor. Soc.*, **141**, 1049–1064, https://doi.org/10.1002/qj.2447.

Jain, D., A. Chakraborty, and R. S. Nanjundaiah, 2018: A mechanism for the southward propagation of mesoscale convective systems over the Bay of Bengal. *J. Geophys. Res. Atmos.*, **123**, 3893–3913, https://doi.org/10.1002/2017JD027470.

Johnson, R. H., 2011: Diurnal cycle of monsoon convection. *The Global Monsoon System: Research and Forecast*, C.-P. Chang, et al., Eds., *World Scientific Series on Asia-Pacific Weather and Climate*, Vol. 5, 2nd ed. World Scientific, 257–276, https://doi.org/10.1142/9789814343411_0015.

Jones, S. C., 1995: The evolution of vortices in vertical shear I: Initially barotropic vortices. *Quart. J. Roy. Meteor. Soc.*, **121**, 821–851, https://doi.org/10.1002/qj.49712152406.

Kiladis, G. N., C. D. Thorncroft, and N. M. Hall, 2006: Three-dimensional structure and dynamics of African easterly waves. Part I: Observations. *J. Atmos. Sci.*, **63**, 2212–2230, https://doi.org/10.1175/JAS3741.1.

Kondo, Y., A. Higuchi, and K. Nakamura, 2006: Small-scale cloud activity over the maritime continent and the western Pacific as revealed by satellite data. *Mon. Wea. Rev.*, **134**, 1581–1599, https://doi.org/10.1175/MWR3132.1.

Krishnamurthy, V., and R. Ajayamohan, 2010: Composite structure of monsoon low pressure systems and its relation to Indian rainfall. *J. Climate*, **23**, 4285–4305, https://doi.org/10.1175/2010JCLI2953.1.

Laing, A. G., R. Carbone, V. Levizzani, and J. Tuttle, 2008: The propagation and diurnal cycles of deep convection in northern tropical Africa. *Quart. J. Roy. Meteor. Soc.*, **134**, 93–109, https://doi.org/10.1002/qj.194.

Liu, C., M. W. Moncrieff, and J. D. Tuttle, 2008: A note on propagating rainfall episodes over the Bay of Bengal. *Quart. J. Roy. Meteor. Soc.*, **134**, 787–792, https://doi.org/10.1002/qj.246.

López, R. E., 1977: The lognormal distribution and cumulus cloud populations. *Mon. Wea. Rev.*, **105**, 865–872, https://doi.org/10.1175/1520-0493(1977)105<0865:TLDACC>2.0.CO;2.

Machado, L. T., M. Desbois, and J.-P. Duvel, 1992: Structural characteristics of deep convective systems over tropical Africa and the Atlantic Ocean. *Mon. Wea. Rev.*, **120**, 392–406, https://doi.org/10.1175/1520-0493(1992)120<0392:SCODCS>2.0.CO;2.

——, J.-P. Duvel, and M. Desbois, 1993: Diurnal variations and modulation by easterly waves of the size distribution of convective cloud clusters over West Africa and the Atlantic Ocean. *Mon. Wea. Rev.*, **121**, 37–49, https://doi.org/10.1175/1520-0493(1993)121<0037:DVAMBE>2.0.CO;2.

Mapes, B., and R. Houze, 1993: Cloud clustures and superclusters over the oceanic warm pool. *Mon. Wea. Rev.*, **121**, 1398–1415, https://doi.org/10.1175/1520-0493(1993)121<1398:CCASOT>2.0.CO;2.

——, T. T. Warner, and M. Xu, 2003: Diurnal patterns of rainfall in northwestern South America. Part III: Diurnal gravity waves and nocturnal convection offshore. *Mon. Wea. Rev.*, **131**, 830–844, https://doi.org/10.1175/1520-0493(2003)131<0830:DPORIN>2.0.CO;2.

Mathon, V., H. Laurent, and T. Lebel, 2002: Mesoscale convective system rainfall in the Sahel. *J. Appl. Meteor.*, **41**, 1081–1092, https://doi.org/10.1175/1520-0450(2002)041<1081:MCSRIT>2.0.CO;2.

Miyakawa, T., and T. Satomura, 2006: Seasonal variation and environmental properties of southward propagating mesoscale convective systems over the Bay of Bengal. *SOLA*, **2**, 88–91, https://doi.org/10.2151/sola.2006-023.

Nakazawa, T., 1988: Tropical super clusters within intraseasonal variations over the western Pacific. *J. Meteor. Soc. Japan*, **66**, 823–839, https://doi.org/10.2151/jmsj1965.66.6_823.

Nguyen, H., and J.-P. Duvel, 2008: Synoptic wave perturbations and convective systems over equatorial Africa. *J. Climate*, **21**, 6372–6388, https://doi.org/10.1175/2008JCLI2409.1.

Prakash, S., C. Mahesh, and R. M. Gairola, 2011: Large-scale precipitation estimation using Kalpana-1 IR measurements and its validation using GPCP and GPCC data. *Theor. Appl. Climatol.*, **106**, 283–293, https://doi.org/10.1007/s00704-011-0435-7.

Rajeevan, M., S. Gadgil, and J. Bhate, 2010: Active and break spells of the Indian summer monsoon. *J. Earth Syst. Sci.*, **119**, 229–247, https://doi.org/10.1007/s12040-010-0019-4.

Ramamurthy, K., 1969: Monsoon of India: Some aspects of the 'break' in the Indian southwest monsoon during July and August. Forecasting Manual FMU Rep. IV-18-3, Comprehensive Articles on Selected Topics, India Meteorological Department, 30 pp., http://www.imdpune.gov.in/Weather/Forecasting_Mannuals/IMD_IV-18.3.pdf.

Rao, Y., 1976: Southwest monsoon. *Meteorological Monograph Synoptic Meteorology*, No. 1, India Meteorological Department, 379 pp., http://imdpune.gov.in/Weather/Reports/sw%20monsoon%20whole%20book.pdf.

Raymond, D., 1992: Nonlinear balance and potential-vorticity thinking at large Rossby number. *Quart. J. Roy. Meteor. Soc.*, **118**, 987–1015, https://doi.org/10.1002/qj.49711850708.

Roca, R., and V. Ramanathan, 2000: Scale dependence of monsoonal convective systems over the Indian ocean. *J. Climate*, **13**, 1286–1298, https://doi.org/10.1175/1520-0442(2000)013<1286:SDOMCS>2.0.CO;2.

——, T. Fiolleau, and D. Bouniol, 2017: A simple model of the life cycle of mesoscale convective systems cloud shield in the tropics. *J. Climate*, **30**, 4283–4298, https://doi.org/10.1175/JCLI-D-16-0556.1.

Rotunno, R., J. B. Klemp, and M. L. Weisman, 1988: A theory for strong, long-lived squall lines. *J. Atmos. Sci.*, **45**, 463–485, https://doi.org/10.1175/1520-0469(1988)045<0463:ATFSLL>2.0.CO;2.

Sahany, S., V. Venugopal, and R. S. Nanjundiah, 2010: Diurnal-scale signatures of monsoon rainfall over the Indian region from TRMM satellite observations. *J. Geophys. Res.*, **115**, D02103, https://doi.org/10.1029/2009JD012644.

Sakaeda, N., G. Kiladis, and J. Dias, 2017: The diurnal cycle of tropical cloudiness and rainfall associated with the Madden–Julian oscillation. *J. Climate*, **30**, 3999–4020, https://doi.org/10.1175/JCLI-D-16-0788.1.

Sanders, F., 1984: Quasi-geostrophic diagnosis of the monsoon depression of 5–8 July 1979. *J. Atmos. Sci.*, **41**, 538–552, https://doi.org/10.1175/1520-0469(1984)041<0538:QGDOTM>2.0.CO;2.

Sikka, D. R., 1978: Some aspects of the life history, structure and movement of monsoon depressions. Monsoon Dynamics, Birkhäuser Basel, 1501–1529, https://doi.org/10.1007/978-3-0348-5759-8_21.

——, 1980: Some aspects of the large scale fluctuations of summer monsoon rainfall over India in relation to fluctuations in the planetary and regional scale circulation parameter. *Proc. Indian Acad. Sci. (Earth Planet. Sci.)*, **89**, 179–195.

Sikka, D., and S. Gadgil, 1978: Large scale rainfall over India during the summer monsoon and its relation to the lower and upper tropospheric vorticity. *Indian J. Hydrol. Geophys.*, **120**, 219–231.

——, and ——, 1980: On the maximum cloud zone and the ITCZ over Indian, longitudes during the southwest monsoon. *Mon. Wea. Rev.*, **108**, 1840–1853, https://doi.org/10.1175/1520-0493(1980)108<1840:OTMCZA>2.0.CO;2.

Sørland, S. L., and A. Sorteberg, 2015: The dynamic and thermodynamic structure of monsoon low-pressure systems during extreme rainfall events. *Tellus*, **67A**, 27039, https://doi.org/10.3402/tellusa.v67.27039.

Stechmann, S. N., and A. J. Majda, 2009: Gravity waves in shear and implications for organized convection. *J. Atmos. Sci.*, **66**, 2579–2599, https://doi.org/10.1175/2009JAS2976.1.

Takayabu, Y. N., 1994: Large-scale cloud disturbances associated with equatorial waves. Part I: Special features of the cloud disturbances. *J. Meteor. Soc. Japan*, **72**, 433–449, https://doi.org/10.2151/jmsj1965.72.3_433.

Trenberth, K. E., D. P. Stepaniak, and J. M. Caron, 2000: The global monsoon as seen through the divergent atmospheric circulation. *J. Climate*, **13**, 3969–3993, https://doi.org/10.1175/1520-0442(2000)013<3969:TGMAST>2.0.CO;2.

Tulich, S. N., and G. N. Kiladis, 2012: Squall lines and convectively coupled gravity waves in the tropics: Why do most cloud systems propagate westward? *J. Atmos. Sci.*, **69**, 2995–3012, https://doi.org/10.1175/JAS-D-11-0297.1.

Wang, C.-C., G. T.-J. Chen, and R. E. Carbone, 2004: A climatology of warm-season cloud patterns over East Asia based on GMS infrared brightness temperature observations. *Mon. Wea. Rev.*, **132**, 1606–1629, https://doi.org/10.1175/1520-0493(2004)132<1606:ACOWCP>2.0.CO;2.

Williams, M., and R. A. Houze, 1987: Satellite-observed characteristics of winter monsoon cloud clusters. *Mon. Wea. Rev.*, **115**, 505–519, https://doi.org/10.1175/1520-0493(1987)115<0505:SOCOWM>2.0.CO;2.

Zuidema, P., 2003: Convective clouds over the Bay of Bengal. *Mon. Wea. Rev.*, **131**, 780–798, https://doi.org/10.1175/1520-0493(2003)131<0780:CCOTBO>2.0.CO;2.